Competing alignments of nematic liquid crystals on square-patterned substrates

ANQUETIL-DECK, C., CLEAVER, Doug <http://orcid.org/0000-0002-4278-0098> and ATHERTON, T. J.

Published version

ANQUETIL-DECK, C., CLEAVER, Doug and ATHERTON, T. J. (2012). Competing alignments of nematic liquid crystals on square-patterned substrates. Physical review E. Statistical, nonlinear and soft matter physics, 86 (4), 041707-1.

Competing alignments of nematic liquid crystals on square-patterned substrates

C. Anquetil-Deck* and D. J. Cleaver†
Materials and Engineering Research Institute, Sheffield Hallam University, City Campus, Howard Street, Sheffield, S1 1WB, United Kingdom

T. J. Atherton
Department of Physics and Astronomy, Center for Nanoscopic Physics, Tufts University, 4 Colby Street, Medford, Massachusetts 02155, USA
(Received 26 June 2012; published 31 October 2012)

A theoretical analysis is presented of a nematic liquid crystal confined between substrates patterned with squares that promote vertical and planar alignment. Two approaches are used to elucidate the behavior across a wide range of length scales: Monte Carlo simulation of hard particles and Frank-Oseen continuum theory. Both approaches predict bistable degenerate azimuthal alignment in the bulk along the edges of the squares; the continuum calculation additionally reveals the possibility of an anchoring transition to diagonal alignment if the polar anchoring energy associated with the pattern is sufficiently weak. Unlike the striped systems previously analyzed, the Monte Carlo simulations suggest that there is no "bridging" transition for sufficiently thin cells. The extent to which these geometrically patterned systems resemble topographically patterned substrates, such as square wells, is also discussed.

DOI: 10.1103/PhysRevE.86.041707 PACS number(s): 61.30.Hn, 61.30.Dk, 07.05.Tp

I. INTRODUCTION

The imposition of a liquid crystal's (LC's) bulk director orientation through that LC's interaction with a confining substrate is termed anchoring [1]. In the absence of defects and applied fields, substrate anchoring is the main determinant of the director profile in a sandwich geometry LC cell; the director profile in such a cell is set through minimization of the orientational elastic energy, subject to each wall's polar and azimuthal anchoring constraints. At a continuum level, this elastic energy is most commonly expressed through square director gradient terms corresponding to the independent splay, twist, and bend modes of orientational deformation, weighted by the elastic constants K_1, K_2, and K_3, respectively. When considered at a finer length scale, conversely, both the anchoring strengths and the bulk elastic constants are emergent from the microscopic interplay of the orientational and positional degrees of freedom of the liquid crystalline molecules and the confining surfaces.

Traditional routes to establishing desired anchoring behaviors, and, thus, director profiles of use for display devices, include substrate rubbing and various photoalignment approaches (light-induced *cis-trans* isomerization, photodegradation, etc.). Although significant empirical knowledge has been developed in relation to each of these approaches, no coherent picture has been established of the molecular mechanisms that underpin continuum concepts such as anchoring angles and coefficients and surface viscosities. Introducing inhomogeneity into substrate conditions has, for some time, been recognized as an alternative route to both controlling conventional anchoring and, increasingly, introducing new phenomena. A range of such substrates have been developed and examined. These cover patterning length scales ranging from 10^{-7} m upward, couple to the LC either sterically, chemically, or dielectrically (or by a combination of same), and have been achieved as both one-dimensional (stripes, ridges, etc.) and two-dimensional (circles, squares, triangles, posts, etc.) patternings.

One of the important phenomena that can be achieved through substrate patterning is bistability, which is stabilization of two distinct anchoring arrangements with (in the absence of an applied field) mutually inaccessible free energy minima. Pattern-stabilized bistability has now been established for the blazed grating structure of zenithally bistable devices [2,3], the two-dimensional array of post-aligned bistable nematic [4] devices, and, more recently, a steric square-well arrangement [5,6]. In each of these, the bistability pertains between one state with a continuous director arrangement and a second containing orientational defects that are pinned in some way by the substrate inhomogeneity. This suggests that the key length scale for achieving bistability here is the size and periodicity of the patterning, a conjecture which is supported by the success of mesoscopic modeling approaches in both accessing the bistable states and relating, semiquantitatively, switching fields to geometrical parameters [7,8].

In addition to these sterically patterned systems, chemical patterning has now also been developed as an approach for imposing substrate inhomogeneity on LC systems. The notion of imposing combinations of azimuthal and polar anchorings on LCs via chemically nanopatterned substrates was the subject of early experimental work [9–11]. Subsequently, Lee and Clark performed a more systematic study of the alignment properties of nematic LCs on surfaces comprising both homeotropic and planar alignment areas [12]. For stripe patterns, they found that the polar orientation depends on the relative areas of the homeotropic and planar regions but that the azimuthal anchoring always runs along the direction of the stripes. Scharf and co-workers [13,14] undertook further investigations of systems with competing alignment regions. Subsequent innovations by the groups of Abbott [15]

*Present address: Karlsruhe Institute of Technology, Institute for Meteorology and Climate Research, Atmospheric Aerosol Research Department (IMK-AAF), Hermann-von-Helmholtz-Platz 1, D-76344 Eggenstein-Leopoldshafen, Germany.
†d.j.cleaver@shu.ac.uk

and Evans [16] centered on the development of patterns of combinations of alkanethiols deposited as self-assembled monolayers (SAMs) on gold. Using microcontact printing, these systems proved capable of achieving highly reproducible surface features with periodicities of tens of micrometers. Square, circular, and striped patterns written on these length scales were, thus, observed using optical microscopy in crossed-polarizer setups. An alternative approach, employing selective ultraviolet irradiation of SAMs, achieved LC-aligning stripe patterns on the submicrometer scale [17].

In Ref. [18], two of the current authors contributed the simulation aspects of a joint experimental and simulation study of LC alignment at a single patterned substrate. In this, it was shown that a range of patterned SAMs can be used to control LC alignment states and domains. For stripe patterns, the LC was found to align parallel to the stripe boundaries for both nanoscale simulation features and micrometer-scale experimental systems. Indeed, despite the significantly different length scales involved, the qualitative behavior seen in simulations of generic molecular models confined using a striped substrate proved entirely consistent with the experimental observations. Specifically, on undergoing isotropic to nematic ordering, all systems proved to be dominated by the homeotropic-aligning substrate regions at the ordering transition, the influence of the planar-aligning regions only becoming apparent well into the nematic phase.

In Ref. [19], we extended our molecular simulation work to consider the behavior of a thin nematic film confined between two identical nanopatterned substrates. Using patterns involving alternating stripes of homeotropic-favoring and homogeneous-favoring substrate, we showed that the polar anchoring angle can be varied continuously from planar to homeotropic by appropriate tuning of the relative stripe widths and the film thickness. For thin films with equal stripe widths, we also observed orientational bridging, with the surface patterning being written in domains which traversed the nematic film. This dual-bridging-domain arrangement broke down with increase in film thickness, however, being replaced by a single tilted monodomain. Strong azimuthal anchoring in the plane of the stripe boundaries was observed for all systems.

Stripe-geometry systems have also been analyzed by the third of the current authors using continuum theory [20–22]. This larger-length-scale work, which built on earlier treatments by Harnau *et al.* [23], has shown that the basis for azimuthal alignment by striped substrates is associated with differences in the Frank elastic constants. Azimuthal anchoring parallel to the stripes corresponds to the LC adopting a configuration comprising twist, splay, and bend deformations; in the other limiting case, bulk alignment perpendicular to the stripes, only splay and bend deformations are required. Experimentally, K_2 is significantly lower than K_1 and K_3 for most nematics, so that parallel anchoring is stable. Monte Carlo estimates of the elastic constants for calamitic particle-based LC simulation models yield similar elastic constant ratios [24], so this phenomenological agreement between the predictions of particle-based and continuum approaches is to be expected.

In this paper, we extend our respective works on stripe-patterned systems by studying the effect of substrates with square patternings on a confined LC film. Experimental studies of such systems include the checkerboard patternings achieved by Bramble [18] and, more recently, Yi [25] and the bistable square-well systems mentioned above [5,6]. With respect to the latter, we note that both Q-tensor [26] and Landau–De Gennes [27] modeling approaches have been used to examine the stable configurations for such systems. From this, diagonally anchored and edge-anchored states have been identified, the former comprising surface region defects.

Here, then, we use both molecular- and continuum-level modeling approaches to investigate the behavior of LC films confined between square-patterned substrates. In Sec. II we present our molecular-level model system and describe the simulation methodology employed. Section III contains the corresponding simulation results. Following this, in Sec. IV we present a continuum-level analysis of anchoring control in systems with square-patterned substrates. Finally, in Sec. V, we compare and combine the findings from these investigations to draw more general conclusions.

II. MOLECULAR MODEL AND SIMULATION DETAILS

We have performed a series of Monte Carlo (MC) simulations of rod-shaped particles confined in slab geometry between two planar walls. Interparticle interactions have been modeled through the hard Gaussian overlap (HGO) potential [28]. Here, the dependence of the interaction potential v^{HGO} on $\hat{\mathbf{u}}_i$ and $\hat{\mathbf{u}}_j$, the orientations of particles i and j, and $\hat{\mathbf{r}}_{ij}$, the interparticle unit vector is

$$v^{\mathrm{HGO}} = \begin{cases} 0 & \text{if } r_{ij} \geqslant \sigma(\hat{\mathbf{r}}_{ij},\hat{\mathbf{u}}_i,\hat{\mathbf{u}}_j), \\ \infty & \text{if } r_{ij} < \sigma(\hat{\mathbf{r}}_{ij},\hat{\mathbf{u}}_i,\hat{\mathbf{u}}_j), \end{cases} \tag{1}$$

where $\sigma(\hat{\mathbf{r}}_{ij},\hat{\mathbf{u}}_i,\hat{\mathbf{u}}_j)$, the contact distance, is given by

$$\sigma(\hat{\mathbf{r}}_{ij},\hat{\mathbf{u}}_i,\hat{\mathbf{u}}_j) = \sigma_0 \left\{ 1 - \frac{\chi}{2} \left[\frac{(\hat{\mathbf{r}}_{ij}.\hat{\mathbf{u}}_i + \hat{\mathbf{r}}_{ij}.\hat{\mathbf{u}}_j)^2}{1+\chi(\hat{\mathbf{u}}_i.\hat{\mathbf{u}}_j)} + \frac{(\hat{\mathbf{r}}_{ij}.\hat{\mathbf{u}}_i - \hat{\mathbf{r}}_{ij}.\hat{\mathbf{u}}_j)^2}{1-\chi(\hat{\mathbf{u}}_i.\hat{\mathbf{u}}_j)} \right] \right\}^{-1/2}. \tag{2}$$

The parameter χ is set by the particle length to breadth ratio $\kappa = \sigma_{\mathrm{end}}/\sigma_{\mathrm{side}}$ via

$$\chi = \frac{\kappa^2 - 1}{\kappa^2 + 1}. \tag{3}$$

Particle-substrate interactions have been modeled using the hard needle–wall potential (HNW) [29]. In this, the particles do not interact directly with the surfaces. Rather the surface interaction is achieved by considering a hard axial needle of length $\sigma_0 k_s$ placed at the center of each particle (see Fig. 1). This gives an interaction

$$v^{\mathrm{HNW}} = \begin{cases} 0 & \text{if } |z_i - z_0| \geqslant \sigma_w(\hat{\mathbf{u}}_i), \\ \infty & \text{if } |z_i - z_0| < \sigma_w(\hat{\mathbf{u}}_i), \end{cases} \tag{4}$$

where z_0 represents the location of a substrate and

$$\sigma_w(\hat{\mathbf{u}}_i) = \tfrac{1}{2}\sigma_0 k_s \sin(\theta_i). \tag{5}$$

Here, k_s is the dimensionless needle length and $\theta_i = \arcsin(u_{i,z})$ is the angle between the substrate plane and the particle's orientation vector. $\theta_i = 0$ corresponds to planar anchoring and $\theta_i = \Pi/2$ corresponds to homeotropic anchoring. For small k_s, the homeotropic arrangement has been shown to be stable, whereas planar anchoring is favored for long

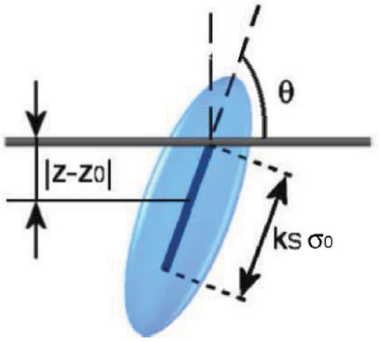

FIG. 1. (Color online) Schematic representation of the geometry used for the HNW particle-substrate interaction [29].

k_s [29]. Furthermore, despite its simplicity, the HNW potential has been found to exhibit qualitatively identical behavior to that obtained using more complex particle-substrate potentials [30]. Here, by imposing variation in k_s across the two boundary walls, we investigate the effects of molecular-scale substrate patterning on LC anchoring. The results presented in Sec. III were obtained for systems of 864 $\kappa = 3$ HGO particles confined between two square-patterned substrates. The substrates were separated by a distance $L_z = 4\kappa\sigma_0$, with periodic boundary conditions being imposed in the x and y directions.

On each substrate, k_s was set to a homeotropic-aligning value ($k_s = 0$) for two quadrants of its area and a planar value ($k_s = 3$) for the remainder. Sharp boundaries have been imposed between the different alignment regions and the patterns on the top and bottom surfaces have been kept in perfect registry with one another, as shown in the schematic in Fig. 2. The simulated system was initialized at low density and compressed, in small increments, by decreasing the box dimensions L_x and L_y while maintaining the condition $L_x/L_y = 1$. At each density, a run length of 10^6 MC sweeps (where one sweep represents one attempted move per particle)

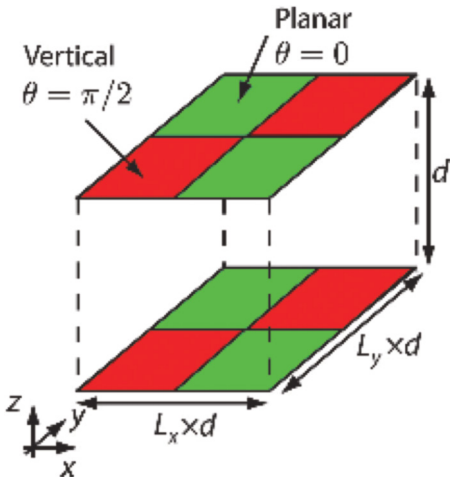

FIG. 2. (Color online) Schematic representation of rectangle-patterned systems with alternating homeotropic-inducing [dark (red online)] and planar-inducing [light (green online)] substrate regions. The Euler angle ϕ is 0 from the y axis.

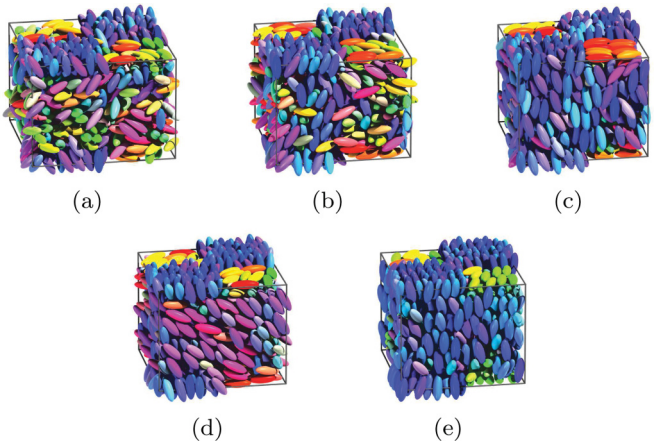

FIG. 3. (Color online) Snapshots of the square-patterned system with sharp transitions between $k_s = 0$ and $k_s = 3$ regions for a series of different reduced densities. Particles are color coded for orientation. (a) $\rho* = 0.30$, (b) $\rho* = 0.34$, (c) $\rho* = 0.37$, (d) $\rho* = 0.38$, and (e) $\rho* = 0.40$.

was performed, with averages and profiles being accumulated for the final 500 000 sweeps.

Analysis was performed by dividing stored system configurations into 100 equidistant constant-z slices and calculating averages of relevant observables in each slice. This yielded profiles of quantities such as number density, $\rho^*(z)$, from which structural changes could be assessed. Orientational order profiles were also calculated, particularly

$$Q_{zz}(z) = \frac{1}{N(z)} \sum_{i=1}^{N(z)} \left(\frac{3}{2} u_{i,z}^2 - \frac{1}{2} \right), \tag{6}$$

which measures variation across the confined films of orientational order measured with respect to the substrate normal. Here $N(z)$ is the instantaneous occupancy of the relevant slice. We have also further subdivided the system to assess lateral inhomogeneities induced by the patterning.

III. MONTE CARLO SIMULATION RESULTS

The outcomes of the square-patterned surface system simulations are summarized by the snapshots shown in Fig. 3. Several remarks emerge from these. The substrate patterning is readily apparent from all of these, with ordered layers of homeotropic-aligned and planar-aligned particles residing in the appropriate regions. Sharp delineation between these regions can be seen for all densities. At $\rho^* = 0.30$ and 0.34, the particles at the center of the film appear to be relatively disordered, whereas aligned monodomains can be seen at the three higher densities. Animations of these simulations show that in the planar-aligning substrate regions, the molecules regularly flipped en masse between the x and y orientations. This tendency is apparent from comparing Figs. 3(c)–3(e); the orientations on the planar parts of the substrate vary from image to image. At $\rho^* = 0.37$, the system appears to exhibit homeotropic anchoring [Fig. 3(c)]. On increasing the density ($\rho^* = 0.38$), however, this initial homeotropic anchoring adopts a clear tilt [Fig. 3(d)] through which the planar-alignment regions on the two substrates become

coupled. On further compression to $\rho^* = 0.40$, the bulk director partially regains its alignment normal to the substrates [Fig. 3(e)]. At the nematic density $\rho^* = 0.38$, the homeotropic and planar substrate regions are restricted to monolayers, with orientational discontinuities being seen between these layers and the tilted bulk anchoring. At high ($\rho^* = 0.40$) and moderate ($\rho^* = 0.37$) densities, where the bulk anchoring was more homeotropic, only the planar parts of the surface monolayers appear orientationally disconnected from the bulk.

In the light of these observations, we have analyzed the behavior of this system more quantitatively by calculating two sets of profiles of key observables; for analysis purposes, each simulated system has been split in two according to the imposed substrate pattern. In this, individual particles have been allocated to homeotropic-confined or homogeneous-confined regions according to their x and y coordinates.

The density profiles depicted in Fig. 4(a) show the adsorption characteristics for the portion of the film confined between the homeotropic surface regions. These indicate that increasing the density leads to formation of surface layers with a periodicity of $\simeq 2\sigma_0$ (i.e., 2/3 of the particle length). Figure 4(b) shows the corresponding behavior of the regions of the film confined between the planar-confining surfaces. Here, a shorter wavelength density modulation is apparent close to the substrates. Despite these differences close to the substrates, both profiles adopt very similar behaviors in the central part of the film: essentially featureless at low (isotropic) densities and weakly oscillatory at high (nematic) densities. These oscillations are consistent with the formation of a homeotropic (or near-homeotropic) bulk monodomain. Such monodomain formation is only seen for much thicker films when stripe patterning is imposed [19]. The weakness of the density modulations, as well as the observation of tilt at some densities, indicates that these systems are not adopting homeotropic orientations simply to commensurate an integer number of layers across the film thickness. Such behavior has been seen previously but only for much thinner LC films [31]. Also, we have found equivalent behaviors for other choices of the wall separation, d [32].

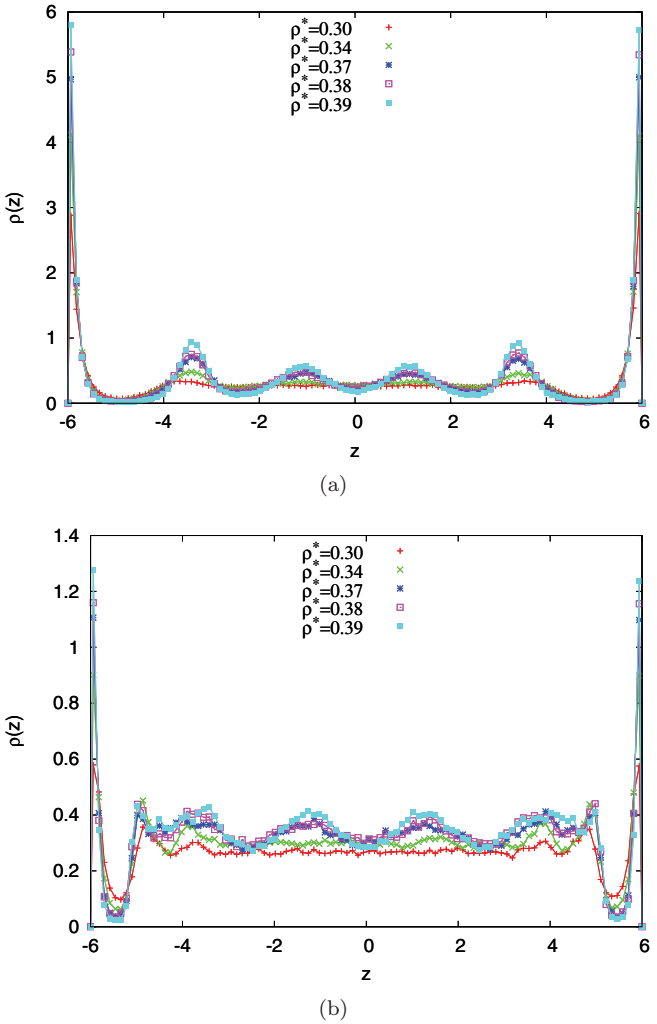

FIG. 4. (Color online) Density profiles for the square-patterned system at different reduced density ρ^*. (a) Density profile: homeotropic-confined region; (b) density profile: planar-confined region.

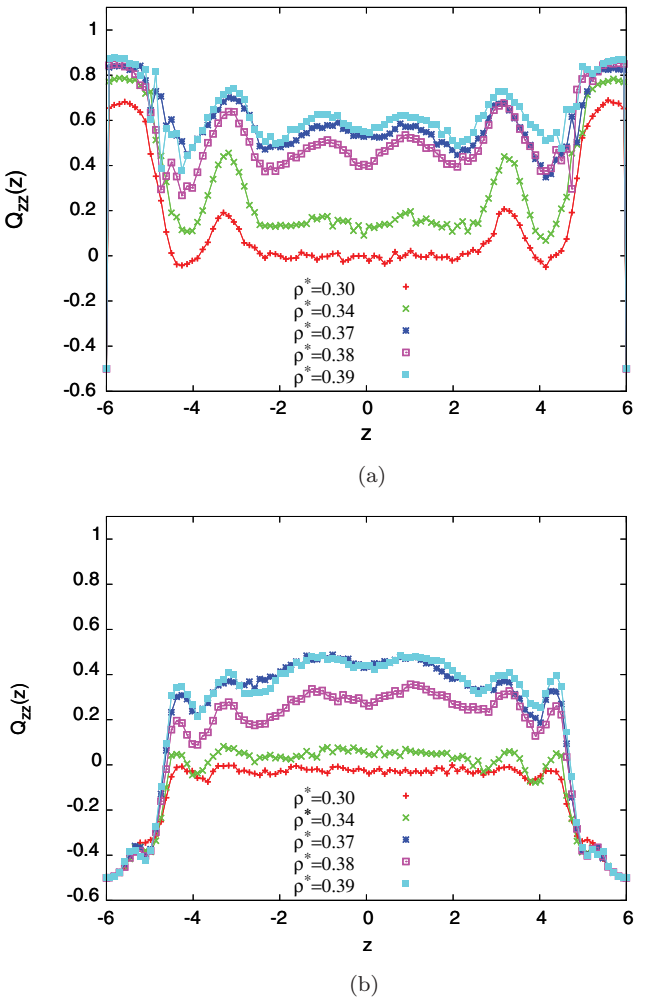

FIG. 5. (Color online) Q_{zz} profiles for the square-patterned system at different reduced density ρ^*. (a) Q_{zz} profile for the homeotropic-confined region; (b) Q_{zz} profile for the planar-confined region.

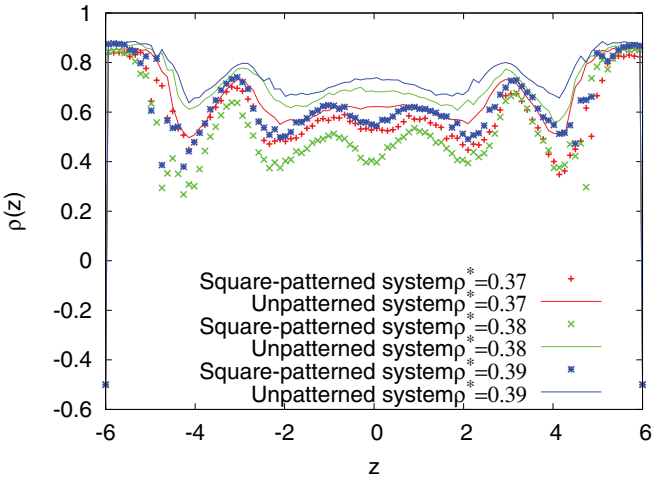

FIG. 6. (Color online) Comparison of the Q_{zz} profiles for unpatterned (lines) and square-patterned (symbols) systems: homeotropic regions.

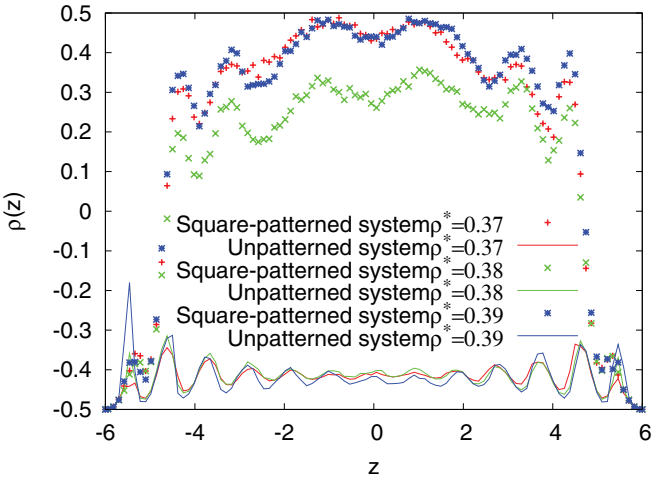

FIG. 7. (Color online) Comparison of the Q_{zz} profiles for unpatterned (lines) and square-patterned (symbols) systems: planar regions.

A more complete understanding of the orientational aspects of the substrate-induced ordering in this system can be obtained from the Q_{zz} diagonal component of the order tensor. For perfect homeotropic anchoring, $Q_{zz}(z)$ should tend to 1 and for perfect planar anchoring, $Q_{zz}(z)$ should tend to -0.5. Figure 5(a) shows the Q_{zz} profiles measured in the homeotropic-confined regions. As the density is increased, initially the bulk-region Q_{zz} value increases as well, showing the development of homeotropic anchoring in the bulk. At a density of 0.37, the bulk Q_{zz} value reaches 0.60–0.65. On further increasing the density to 0.38, however, the Q_{zz} value decreases to just below 0.5. Then, as the density reaches 0.4, the Q_{zz} value increases again to $Q_{zz} = 0.60$–0.65. This nonmonotonic behavior confirms, in a statistically significant fashion, the tilt behavior apparent in the corresponding snapshots.

It is also informative to compare these observations with equivalent profiles obtained for HGO films confined between unpatterned homeotropic- and planar-aligning substrates. To this end, Fig. 6 shows that, for the equivalent unpatterned homeotropic-aligning system, increasing the density causes the central Q_{zz} value to increase monotonically. The fact that Q_{zz} shows a decrease at $\rho^* \simeq 0.37$ in the patterned system is, then, associated with a tilt of the bulk director caused by the presence of the planar pattern regions on the surface.

An equivalent comparison performed for the planar-aligning region (Fig. 7) shows a very marked difference between the patterned and unpatterned systems. Indeed, despite its intrinsic anchoring character, the $Q_{zz}(z)$ behavior of the planar-aligned region of the patterned system is actually far closer to that of the unpatterned homeotropic-confined system. Only very close to the substrates is the planar nature of the imposed substrate pattern apparent.

In order to assess the azimuthal anchoring behavior in this system, we have constructed a time-averaged histogram of the molecular azimuthal angles observed during the $\rho^* = 0.37$ simulation. Specifically, this histogram (Fig. 8) was generated from 500 stored configuration files and based on the orientations of particles within $1\sigma_0$ of the planar substrate regions. The histogram is strongly peaked at angles corresponding to the boundaries of the square pattern; i.e., the molecules at the planar substrates are strongly disposed to adopting azimuthal angles ϕ of $\simeq 0^\circ \leqslant \phi \leqslant 5^\circ$ and $\simeq 85^\circ \leqslant \phi \leqslant 90^\circ$. This is consistent with our previous observation that the molecules on this region appeared to regularly flip between the x and y directions.

Before closing this section, we return to the observation that, other than in cases where the two were coincident, the substrate patterning applied here failed to penetrate the LC film beyond the first adsorbed monolayer. We can report that this was actually a general characteristic observed for a range of different two-dimensional patternings; simulations we have performed with circle, oval, and rectangle patterns and a range of film thicknesses have all led to the development of central monodomain configurations [32]. This differs qualitatively from what has been observed for thin LC films confined between stripe-patterned substrates [19], where the substrate patterning is written across the film in bridging domains. Indeed, both the bulk monodomain formed here by the

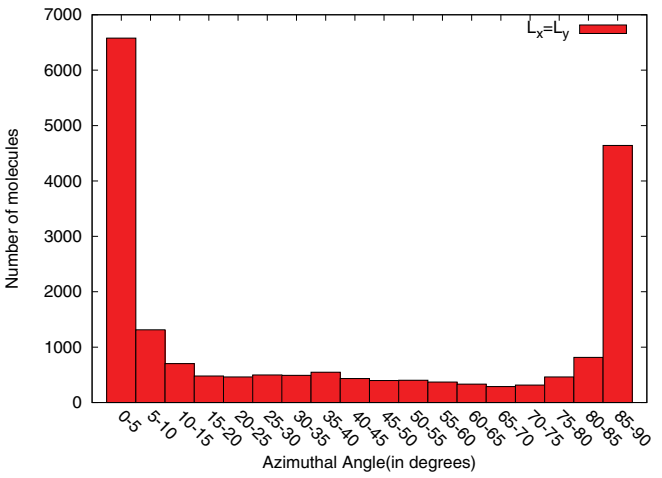

FIG. 8. (Color online) Histogram showing the azimuthal angle distribution of surface particles in the planar-aligned region.

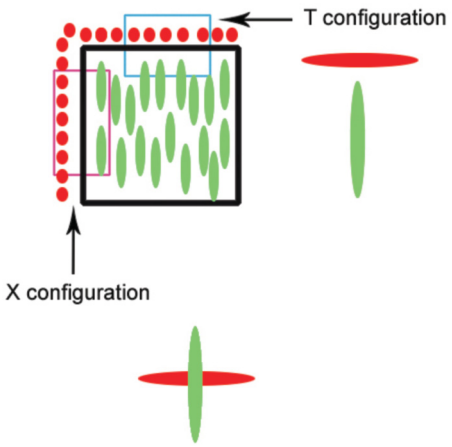

FIG. 9. (Color online) Schematic x-y plane slice through a hypothetical planar-aligned bridging domain in a square-patterned system. T configuration: splay and bend distortion. X configuration: twist.

square-patterned film and its nonmonotonic tilt dependence on density are equivalent to the behavior seen only for much thicker stripe-patterned films.

To explain why the orientational bridging observed in thin stripe-patterned systems is lost on moving to two-dimensional patterns, we consider the hypothetical square bridging domain shown schematically in Fig. 9. Here a planar-aligned domain is bounded at each face by homeotropic material. From the schematic, though, it is clear that two distinct pairs of domain boundaries would be required for this situation: one pair involving T-like orientational changes and another involving X-like configurations. Such a scenario is clearly unstable since the symmetry change across the interface is spatially inhomogeneous. As a consequence, the hypothetical square bridging domain considered here could never be a stable arrangement. Indeed, similar stability arguments disallow all orientational monodomain bridges projected from two-dimensional patternings.

To conclude, these simulations indicate that LC film confined between square-patterned substrates have a tendency to form monodomains. These monodomains are different from those developed between unpatterned substrates, though, since (a) they can exhibit a nonmonotonic density-dependent tilt and (b) the azimuthal anchoring shows a strong coupling parallel to the square edges but is degenerate between the different edge orientations.

IV. CONTINUUM MODEL

To further understand the aligning effects observed in the simulations presented in the previous section, we now consider the behavior of systems with the same geometry of patterning but applied at a much larger length scale. Specifically, we analyze the effect of square-patterned substrates on LC films in the continuum limit. In this approach, the local orientation of the nematic is characterized by a unit vector field known as the director and parametrized here by

$$\hat{\mathbf{n}}(\mathbf{r}) = (\cos\theta \sin\phi, \cos\theta\cos\phi, \sin\theta), \tag{7}$$

where the coordinates are chosen as depicted in Fig. 2. The actual configuration adopted by the nematic is that which minimizes the Frank free energy

$$F = \frac{1}{2}\int d^3\mathbf{r}\, K_1(\nabla\cdot\hat{\mathbf{n}})^2 + K_2[\hat{\mathbf{n}}\cdot(\nabla\times\hat{\mathbf{n}})]^2 + K_3|\hat{\mathbf{n}} \times(\nabla\times\hat{\mathbf{n}})|^2 + \int_s dS\, g(\vec{\mathbf{n}},\vec{\mathbf{n}}_0). \tag{8}$$

Here, the first integral is to be performed over the volume of the nematic layer and the second over the surfaces in contact with the substrate. The interaction of the nematic with the surface is characterized by an anchoring potential $g(\vec{\mathbf{n}},\vec{\mathbf{n}}_0)$ that measures the energy cost of moving the director away from an easy axis $\vec{\mathbf{n}}_0$; for a patterned surface this varies as a function of position. The configuration of the LC is found by solving the Euler-Lagrange equations for θ and ϕ; these are generally nonlinear and difficult to solve analytically in more than one spatial dimension.

A common simplification, known as the one-constant approximation, is to set $K_1 = K_2 = K_3$. If this is done, the Euler-Lagrange equation for θ reduces to Laplace's equation. However, such an approximation is unsuitable for analyzing situations with patterned surfaces because the aligning effect on the LC is due to *differences* between the elastic constants [20]. A "two-constant" approximation, where $K_1 = K_3 \neq K_2$ has been previously used to understand the situation of a nematic film in contact with a surface patterned with alternating homeotropic and planar stripes, a two-dimensional system [20,22], and here we extend the analysis to three dimensions.

In order to proceed, a further simplifying assumption is made: that the director is confined everywhere to a single plane, i.e., that ϕ is spatially uniform. This simplification is motivated (and justified) by the observation that the molecular distribution of azimuthal angles (Fig. 8) in our MC simulations implies a monodomain arrangement for all nematic films confined in this way. While ϕ is taken to be constant, the polar, or tilt, angle θ remains free to vary in response to the substrate pattern. Keeping ϕ fixed is further motivated by the observation that wherever the director is nearly homeotropic, variations in ϕ contribute negligibly to the free energy. The free energy density in this situation is

$$f = \frac{1}{2}\left\{(\tau\cos^2\phi + \sin^2\phi)\left(\frac{\partial\theta}{\partial x}\right)^2 + (\tau\sin^2\phi + \cos^2\phi) \times \left(\frac{\partial\theta}{\partial y}\right)^2 + (1-\tau)\sin(2\phi)\frac{\partial\theta}{\partial x}\frac{\partial\theta}{\partial y} + \left(\frac{\partial\theta}{\partial z}\right)^2\right\}, \tag{9}$$

where $\tau = K_2/K_1$ and the corresponding Euler-Lagrange equation for θ is linear:

$$(\tau\cos^2\phi + \sin^2\phi)\frac{\partial^2\theta}{\partial x^2} + (\tau\sin^2\phi + \cos^2\phi)\frac{\partial^2\theta}{\partial y^2} + (1-\tau)\sin(2\phi)\frac{\partial^2\theta}{\partial x\partial y} + \frac{\partial^2\theta}{\partial z^2} = 0. \tag{10}$$

This can be converted to Laplace's equation in new coordinates (ξ,η,ζ) by the following linear transformation:

$$\begin{pmatrix}\xi\\ \eta\\ \zeta\end{pmatrix} = P^T Q P \begin{pmatrix}x\\ y\\ z\end{pmatrix}, \tag{11}$$

where

$$P = \begin{pmatrix}\cos\left(\phi+\frac{\pi}{4}\right) & -\sin\left(\phi+\frac{\pi}{4}\right) & 0\\ \sin\left(\phi+\frac{\pi}{4}\right) & \cos\left(\phi+\frac{\pi}{4}\right) & 0\\ 0 & 0 & 1\end{pmatrix} \tag{12}$$

and

$$Q = \begin{pmatrix}\frac{1}{2}\left(1+\frac{1}{\sqrt{\tau}}\right) & \frac{1}{2}\left(\frac{1}{\sqrt{\tau}}-1\right) & 0\\ \frac{1}{2}\left(\frac{1}{\sqrt{\tau}}-1\right) & \frac{1}{2}\left(1+\frac{1}{\sqrt{\tau}}\right) & 0\\ 0 & 0 & 1\end{pmatrix}. \tag{13}$$

The geometric interpretation of the transformation is a combination of a rotation and shear. To solve the Euler-Lagrange equation for $\theta(x,y,z)$, Eq. (10), we try a solution of the form

$$\theta(x,y,z) = \theta_0 + \sum_{n=-\infty}^{\infty}\sum_{m=-\infty}^{\infty}\frac{1}{\lambda}(A_{nm}e^{-\nu_{nm}z} + B_{nm}e^{\nu_{nm}z})\exp[i2\pi(nx+my)/\lambda], \tag{14}$$

where $\lambda = 2L_x/d$ such that λd is the period of the patterning in both x and y directions. The equation is satisfied if the parameters ν_{nm} are chosen as

$$\nu_{nm} = \pi\sqrt{2(\tau+1)(m^2+n^2) - 2(\tau-1)[2mn\sin(2\phi)+\cos(2\phi)(m^2-n^2)]}. \tag{15}$$

The constant θ_0 is, from the mean-value theorem,

$$\theta_0 = \frac{\pi}{4}. \tag{16}$$

The coefficients A_{nm} and B_{nm} are determined by the boundary conditions. For weak anchoring, these are from the torque-balance equation

$$\hat{\mathbf{s}}\cdot\frac{\partial f(\theta,\nabla\theta)}{\partial\nabla\theta} + \frac{\partial g(\theta,\theta_e)}{\partial\theta} = 0 \tag{17}$$

evaluated at each surface, where $\hat{\mathbf{s}}$ is the outward surface normal. To facilitate separation of the coefficients in Eq. (16), the harmonic anchoring potential

$$g_H(\theta,\theta_e) = \frac{W_\theta}{2}(\theta-\theta_e)^2 \tag{18}$$

is chosen, yielding the Robin boundary condition

$$\pm L_\theta\frac{\partial\theta}{\partial z} + \theta = \theta_e, \tag{19}$$

where W_θ is the polar anchoring coefficient, $\theta_e(x,y)$ is the spatially varying easy axis promoted by the pattern, the minus sign corresponds to $z = z_0 = -d/2$, the plus sign corresponds to $z = z_0 = +d/2$, and the dimensionless parameter associated with polar anchoring L_θ is

$$L_\theta = \frac{K_1}{W_\theta d}. \tag{20}$$

Inserting the solution (14) into the boundary condition (19) at each surface yields the coupled system of equations

$$\begin{pmatrix}1+L_\theta\nu_{nm} & 1-L_\theta\nu_{nm}\\ e^{-\nu_{nm}}(1-L_\theta\nu_{nm}) & e^{\nu_{nm}}(1+L_\theta\nu_{nm})\end{pmatrix}\begin{pmatrix}A_{nm}\\ B_{nm}\end{pmatrix} = \begin{pmatrix}c_{nm}\\ d_{nm}\end{pmatrix}, \tag{21}$$

where c_{nm} and d_{nm} are the Fourier coefficients of the easy axis profile $\theta_0(x,y)$ at the $z=-d/2$ and $z=+d/2$ surfaces, respectively. These are simply

$$c_{nm} = d_{nm} = \begin{cases}-\frac{\lambda}{\pi nm}, & n,m \text{ odd},\\ 0, & \text{otherwise},\end{cases} \tag{22}$$

and solution of (21) yields

$$\begin{aligned}A_{nm} &= \frac{e^{\nu_{nm}}c_{nm}}{L_\theta\nu_{nm}(e^{\nu_{nm}}-1)+(e^{\nu_{nm}}+1)},\\ B_{nm} &= \frac{c_{nm}}{L_\theta\nu_{nm}(e^{\nu_{nm}}-1)+(e^{\nu_{nm}}+1)}.\end{aligned} \tag{23}$$

The complete director profile for given values of ϕ, τ, L_θ, and λ is then fully specified by the series solution (14) and the parameters (15) and (23) that have now been determined.

The free energy associated with the solution (14) may be evaluated by substituting it into the free energy (9) and performing necessary integrations. The bulk energy is

$$\begin{aligned}F_b = &\sum_{nm}\frac{\pi^2}{\lambda^2\nu_{nm}}\left[\left(A_{nm}^2e^{-\nu_{nm}} + B_{nm}^2e^{+\nu_{nm}}\right)\sinh(\nu_{nm})\right.\\ &\left.+2A_{nm}B_{nm}\nu_{nm}\right]\{(1+\tau)(m^2+n^2)\\ &+(1-\tau)[\cos(2\phi)(m^2-n^2)+2mn\sin(2\phi)]\}\\ &+\sum_{nm}\frac{1}{2}\nu_{nm}\left[\left(A_{nm}^2e^{-\nu_{nm}} + B_{nm}^2e^{+\nu_{nm}}\right)\sinh(\nu_{nm})\right.\\ &\left.-2A_{nm}B_{nm}\nu_{nm}\right].\end{aligned} \tag{24}$$

The surface energy (for each surface) is

$$F_s = \pi^2\lambda^2/16 + \frac{1}{L_\theta}\sum_{nm}(A_{nm}+B_{nm})(A_{nm}+B_{nm}-2c_{nm}). \tag{25}$$

These expressions for the free energy have been evaluated numerically as a function of ϕ for different values of L_θ. A value of $\tau = K_2/K_1 = 1/2$ was used that is approximately

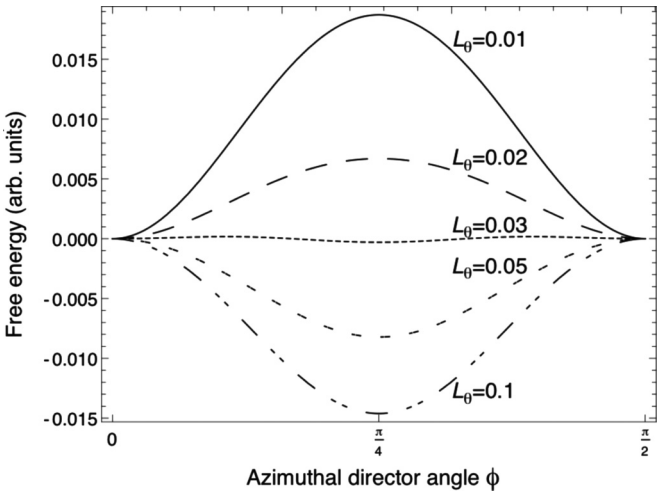

FIG. 10. Free energy of the nematic as a function of ϕ, plotted for $\lambda = 1.0$ and various values of L_θ.

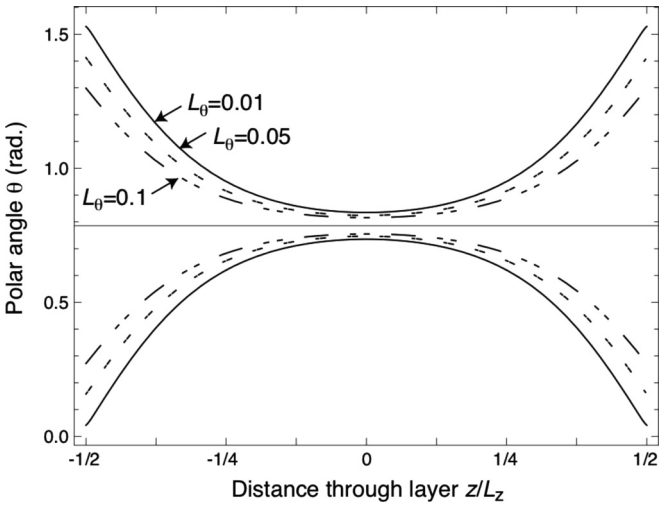

FIG. 12. Calculated director angle profiles $\theta(z)$ in the center of the homeotropic and planar regions, for various values of L_θ.

valid for many common nematics including 5CB. The period of the pattern was initially chosen to be the same as the cell thickness, i.e., $\lambda = 1$. The plots displayed in Fig. 10 reveal an anchoring transition: as $L_\theta \to 0$, representing rigid polar anchoring, the squares promote azimuthal alignment parallel to their sides, and there are two degenerate solutions at $\phi = 0$ or $\phi = \pi/2$, i.e., the same behavior as was observed in our molecular simulations. If L_θ is increased, however, alignment along the diagonals, i.e., $\phi = \pm\pi/4$, becomes the energetically preferred solution. The critical L_θ at which the diagonal and aligned solutions become degenerate is roughly $L_\theta \sim 0.03$. Experiments performed using a single square-patterned substrate have exhibited the $\phi = \pm\pi/4$ behavior corresponding to weak anchoring [18].

The second parameter of interest is λ, the overall size of the squares relative to the cell thickness. Shown in Fig. 11 is the energy difference between the aligned $\phi = 0$ and diagonal $\phi = \pi/4$ solutions as a function of λ, plotted for various values of L_θ. In this plot, therefore, the diagonal solution is stable

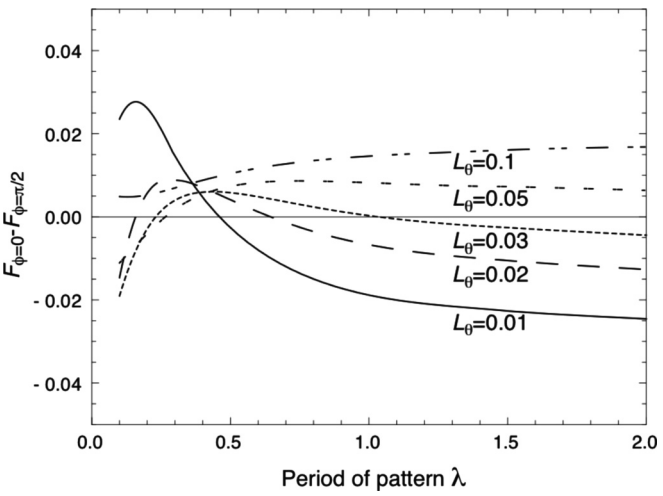

FIG. 11. Free energy difference between the aligned $\phi = 0$ and diagonal $\phi = \pi/4$ solutions as a function of the period of the pattern, λ.

where lines lie below the abscissa, whereas the edge-aligned solution is stable where the lines take positive values. We see, therefore, that for $L_\theta \simeq 0.03$ the diagonally aligned solution is preferred both at small λ and as $\lambda \to \infty$. Reducing L_θ has the effect of narrowing the window of λ values for which the diagonal solution is preferred. Our high-density MC simulation corresponds to a value of $\lambda = 1.12$ (Fig. 11).

Continuum predictions for director tilt profiles as a function of z for the planar and homeotropic regions are displayed in Fig. 12 and show that a nearly uniform configuration is adopted at the cell center. This is in reasonable agreement with the findings from our particle-based simulations, given the very different spatial resolutions accessible to the two methods used. As the inverse anchoring parameter L_θ is increased, the tilt conditions at the substrates relax and the central uniform region widens

V. CONCLUSIONS

Alignment of a nematic between two substrates patterned with alternating homeotropic and planar squares has been studied using two theoretical approaches: MC simulation of rigid particles interacting through the hard Gaussian overlap potential and a calculation performed with nematic continuum theory. Both techniques show a regime where the nematic azimuthally aligns in the bulk with the edge of the squares. In the MC simulations, the average azimuthal orientation of the molecules is observed to flip between the two sides during the runs; these states are energetically degenerate in the continuum approach. Furthermore, the continuum calculation reveals the existence of an anchoring transition. If the polar anchoring is sufficiently weak and the period of the pattern is somewhat greater than the cell thickness, the nematic instead aligns along the diagonals. Unlike previously considered systems of square posts and wells [26,27] our calculations raise the possibility of re-entrant behavior as a function of the period of the pattern: for appropriate values of the polar anchoring energy, the diagonal state becomes unstable at both short- and long-wavelength patterning (Fig. 11). It is likely that the location of the

critical values of the period are only approximately correct because azimuthal variations of the director were not included in our minimization of the free energy. We expect diagonal arrangements to be accessible to the MC approach for larger patterning periodicities; we are presently examining such systems. Equivalently, a transition between the two regimes ought to be experimentally observable by adjusting the ratio of the period of the pattern to the cell thickness.

Our continuum analysis also reveals the surprising result that an exact linear form of the nematic Euler-Lagrange equations exists even if there is three-dimensional variation in the director and the nematic has inhomogeneous elastic constants. The form of the resulting equation lends a geometric interpretation to elastic anisotropy as a transformation into skewed coordinates. This result should be of utility for further study of LC behavior in complicated geometries.

The behavior observed in the present system is qualitatively quite different from that seen where a nematic is aligned between equivalent striped substrates. Previous MC simulations show that, for a sufficiently thin film with stripe-patterned boundaries, there exists a regime where the nematic is divided into domains of vertical and planar alignment that bridge between the corresponding substrate regions. No such bridging behavior was observed for the square-patterned system considered here. Instead, there was a clear tendency for the orientations imposed by the surface patterning to be confined to the first monolayer adsorbed at the substrate. The absence of orientational bridging domains in two-dimensional-patterned systems can be explained by consideration of the spatially inhomogeneous domain boundaries they would imply. Whereas arrangements involving some splaylike and some twistlike domain boundaries in bulk are not stable, these mixed arrangements are seen in the at-substrate monolayers. The line tensions associated with these different geometries presumably have differing energy densities. Despite this, these linear features persist for the strong-anchoring scenario considered in our MC simulations, rather than being displaced subsurface. Since similar behavior appears from both simulation and continuum theory, despite the fact that the latter entirely neglects variations in ordering, it appears that the line tension depends primarily on elastic distortion of the director and does not significantly depend on the scalar order parameter. This justifies use of the continuum theory for such systems.

When deeply in one or other of its possible regimes, edge or diagonal, the alignment in these systems is degenerate due to the symmetry and hence of interest for electro-optic, display, and sensing applications. There is, though, also a capacity for bistabiliity between the edge and diagonal states. In this respect these systems are quite similar to the post-aligned bistable display [26] and the arrays of square wells [27] previously studied. Although these have the same symmetry as the systems considered here, there is an important difference: in the present case the bistable states have no disclinations present in the nematic configuration. Our results indicate, therefore, that bistability is *not* contingent on the presence of defects.

Despite the apparent simplicity of the geometry, our results illustrate the rich phase diagrams exhibited by complex fluids in patterned geometries. Further study of related systems is presently being undertaken, to identify optimal switching strategies between the bistable states identified here.

ACKNOWLEDGMENTS

This work was supported by the Engineering and Physical Research Council, Grant No GR/S59833/01. We acknowledge useful conversations with Steve Evans, Jim Henderson, Jon Bramble, Chris Care, Tim Spencer, and Paulo Teixeira which have been beneficial to our understanding of the systems studied here.

[1] B. Jérôme, Rep. Prog. Phys. **54**, 391 (1991).
[2] J. C. Jones, S. Beldon, E. Wood, P. Brett, M. Francis, and M. Goulding, Dig. Tech. Pap.—Soc. Inf. Disp. Int. Symp. **34**, 954 (2003).
[3] C. V. Brown, M. J. Towler, V. C. Hui, and G. P. Bryan-Brown, Liq. Cryst. **27**, 233 (2000).
[4] S. Kitson and A. Geisow, Appl. Phys. Lett. **80**, 3635 (2002).
[5] C. Tsakonas, A. J. Davidson, C. V. Brown, and N. J. Mottram, Appl. Phys. Lett. **90**, 111913 (2007).
[6] G. G. Wells and C. V. Brown, Appl. Phys. Lett. **91**, 223506 (2007).
[7] T. J. Spencer, C. M. Care, R. M. Amos, and J. C. Jones, Phys. Rev. E **82**, 021702 (2010).
[8] M. V. Yakutovich, C. M. Care, C. J. P. Newton, and D. J. Cleaver, Phys. Rev. E **82**, 041703 (2010).
[9] D. W. Berreman, Phys. Rev. Lett. **28**, 1683 (1972).
[10] T. Z. Qian and P. Sheng, Phys. Rev. Lett. **77**, 4564 (1996).
[11] T. Z. Qian and P. Sheng, Phys. Rev. E **55**, 7111 (1997).
[12] B. Lee and N. A. Clark, Science **291**, 2576 (2001).
[13] S. Park, C. Padeste, H. Schift, J. Gobrecht, and T. Scharf, Adv. Mater. **17**, 1398 (2005).
[14] T. Scharf, S. Park, C. Padeste, H. Schift, N. Basturk and J. Grupp, Mol. Cryst. Liq. Cryst. **438**, 55/[1619] (2005).
[15] R. A. Drawhorn and N. L. Abbott, J. Phys. Chem. **99**, 16511 (1995).
[16] Y. L. Cheng, D. N. Batchelder, S. D. Evans, J. R. Henderson, J. E. Lydon, and S. D. Ogier, Liq. Cryst. **27**, 1267 (2000).
[17] I. H. Bechtold and E. A. Oliveira, Liq. Cryst. **32**, 343 (2005).
[18] J. P. Bramble, S. D. Evans, J. R. Henderson, C. Anquetil, D. J. Cleaver, and N. J. Smith, Liq. Cryst. **34**, 1059 (2007).
[19] C. Anquetil-Deck and D. J. Cleaver, Phys. Rev. E **82**, 031709 (2010).
[20] T. J. Atherton and J. R. Sambles, Phys. Rev. E **74**, 022701 (2006).
[21] T. J. Atherton, J. R. Sambles, J. P. Bramble, J. R. Henderson, and S. D. Evans, Liq. Cryst. **36**, 353 (2009).
[22] T. J. Atherton, Liq. Cryst. **37**, 1225 (2010).
[23] L. Harnau, S. Kondrat, and A. Poniewierski, Phys. Rev. E **76**, 051701 (2007).
[24] M. P. Allen, Mol. Phys. **96**, 1391 (1999).

[25] Y. Yi, V. Khire, C. Bowman, J. Maclennan, and N. Clark, J. Appl. Phys. **103**, 093518 (2008).
[26] S. Cornford and C. J. P. Newton, Hewlett-Packward Laboratories 143R1, 2011.
[27] C. Luo, A. Majumdar, and R. Erban, Phys. Rev. E **85**, 061702 (2012).
[28] P. Padilla and E. Velasco, J. Chem. Phys. **106**, 10299 (1997).
[29] D. J. Cleaver and P. I. C. Teixeira, Chem. Phys. Lett. **338**, 1 (2001).
[30] F. Barmes and D. J. Cleaver, Phys. Rev. E **69**, 061705 (2004).
[31] T. Gruhn and M. Schoen, Phys. Rev. E **55**, 2861 (1997).
[32] C. Anquetil-Deck, Ph.D. thesis, Sheffield Hallam University, 2008.